

Energy doubling of 42 GeV electrons in a metre-scale plasma wakefield accelerator

Ian Blumenfeld¹, Christopher E. Clayton², Franz-Josef Decker¹, Mark J. Hogan¹, Chengkun Huang², Rasmus Ischebeck¹, Richard Iverson¹, Chandrashekhar Joshi², Thomas Katsouleas³, Neil Kirby¹, Wei Lu², Kenneth A. Marsh², Warren B. Mori², Patric Muggli³, Erdem Oz³, Robert H. Siemann¹, Dieter Walz¹ & Miaomiao Zhou²

The energy frontier of particle physics is several trillion electron volts, but colliders capable of reaching this regime (such as the Large Hadron Collider and the International Linear Collider) are costly and time-consuming to build; it is therefore important to explore new methods of accelerating particles to high energies. Plasma-based accelerators are particularly attractive because they are capable of producing accelerating fields that are orders of magnitude larger than those used in conventional colliders^{1–3}. In these accelerators, a drive beam (either laser or particle) produces a plasma wave (wakefield) that accelerates charged particles^{4–11}. The ultimate utility of plasma accelerators will depend on sustaining ultrahigh accelerating fields over a substantial length to achieve a significant energy gain. Here we show that an energy gain of more than 42 GeV is achieved in a plasma wakefield accelerator of 85 cm length, driven by a 42 GeV electron beam at the Stanford Linear Accelerator Center (SLAC). The results are in excellent agreement with the predictions of three-dimensional particle-in-cell simulations. Most of the beam electrons lose energy to the plasma wave, but some electrons in the back of the same beam pulse are accelerated with a field of ~ 52 GV m⁻¹. This effectively doubles their energy, producing the energy gain of the 3-km-long SLAC accelerator in less than a metre for a small fraction of the electrons in the injected bunch. This is an important step towards demonstrating the viability of plasma accelerators for high-energy physics applications.

In a plasma wakefield accelerator large-amplitude electric fields result from space-charge waves excited by the passage of an ultra-relativistic electron beam through a plasma¹². A fully ionized plasma can be formed in a neutral vapour when the radial electric field of the electron beam exceeds the field ionization threshold¹³. The ionization front produces a plasma that has a radius much larger than the beam itself. If the beam density exceeds the plasma density, the plasma electrons are expelled from the volume of the electron pulse, leaving a column of more massive ions behind¹⁴. Subsequently, the expelled plasma electrons are pulled back (by the ions) to the beam axis behind the pulse, overshoot, and set up a space-charge oscillation or wake. The longitudinal field of this wake varies continuously along the pulse, decelerating its core but accelerating the particles in the back. The ion column also provides a focusing force¹⁵ that guides the beam over many diffraction lengths, allowing an efficient transfer of the beam energy to the wake. This force also causes the transverse size of the beam to oscillate as it propagates through the plasma—the so-called betatron oscillations (see Supplementary Movie 1).

Recent plasma wakefield accelerator experiments have shown high-gradient acceleration of electrons using a 10-cm-long plasma¹¹. To obtain energy gains of interest to high-energy physics, these high gradients must be extended over metre-scale plasmas. Such an extension transitions the plasma wakefield accelerator from a regime in which the drive beam has no time to distort, deplete or go unstable, to a regime in which it is significantly depleted in energy, deformed owing to combined effects of diffraction and multiple transverse oscillations, and possibly goes unstable because of the electron-hose instability¹⁶. This work is in this latter regime.

A schematic of the experimental set-up is shown in Fig. 1. In the present work carried out at the Final Focus Test Beam facility at SLAC, the nominally 50-femtosecond-long electron beam containing 1.8×10^{10} particles is focused to a spot size of ~ 10 μm at the entrance of an 85-cm-long column of lithium vapour with a density n_e of 2.7×10^{17} cm⁻³. The nominally 42 GeV beam has a correlated energy spread of approximately 1.5 GeV, with electrons in the front of the beam at higher energies than those at the back. The beam exiting the plasma traverses a metre-long dipole magnet, which disperses the beam electrons according to their energy. The transverse distribution of the dispersed electrons is measured at two distances (planes 1 and 2 in Fig. 1) downstream of the dipole magnet to distinguish the energy changes of the electrons from their possible transverse deflection due to the plasma.

Images of the dispersed electrons are recorded along with the relevant beam parameters on a shot-to-shot basis. The energy gain achieved for each shot is determined as described in the Methods section. Figure 2 shows one example of the electron energy

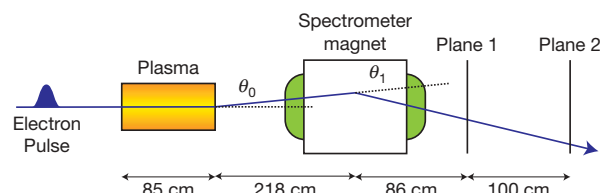


Figure 1 | Schematic of the experimental set-up. Two cameras record the energy-dispersed images at planes 1 and 2. A combination of low dispersion at plane 1 and a lower lens magnification on the camera allows a broad energy spectrum of the beam, including energy gain and loss, to be recorded. A higher dispersion at plane 2 coupled with a larger lens magnification is used to record images showing greater detail of the energy gain. The comparison of these two images allows for an independent measurement of vertical deflection and energy gain, as discussed in the Methods section.

¹Stanford Linear Accelerator Center, 2575 Sand Hill Road, Menlo Park, California 94025, USA. ²University of California Los Angeles, 405 Hilgard Avenue, Los Angeles, California 90095, USA. ³University of Southern California, University Park, Los Angeles, California 90089, USA.

distribution between 35 and 100 GeV after traversing the plasma. The angle θ_0 at the plasma exit for this particular event was calculated to be smaller than $100 \mu\text{rad}$, which is negligible; therefore energy relates directly to position. The highest electron energy is $85 \pm 7 \text{ GeV}$, indicating that some electrons in the tail of the beam with an initial energy of 41 GeV have more than doubled their initial energy. The implied peak accelerating field of $\sim 52 \text{ GV m}^{-1}$ is consistent with the fields previously measured in a 10-cm-long plasma¹¹, indicating that the energy gain is scalable by extending the length of the plasma at least up to 85 cm. With this plasma length, in a series of 800 events, 30% showed an energy gain of more than 30 GeV. Variations in the measured energy gain were correlated to fluctuations in the peak current of the incoming electron beam.

When the length of the lithium vapour column was extended from 85 cm to 113 cm, the maximum energy in an event with a similar incoming current profile was measured to be $71 \pm 11 \text{ GeV}$. Less than 3% of a sample of 800 consecutive events showed an energy gain of more than 30 GeV. There are three possible reasons for this apparent saturation of energy gain observed in the experiment. The first is that the energy of the particles that produced the wake has been depleted to almost zero, such that the acceleration is terminated in the last 28 cm of the plasma. However, the minimum energy measured at

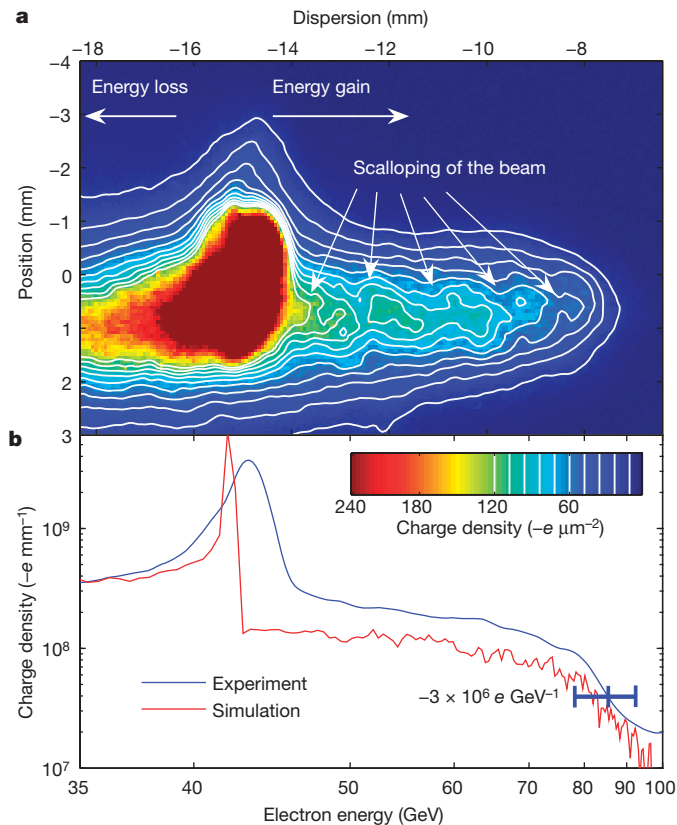


Figure 2 | Energy spectrum of the electrons. **a**, Energy spectrum of the electrons in the 35–100 GeV range as observed in plane 2. The dispersion (shown on the top axis) is inversely proportional to the particle energy (shown on the bottom axis). The head of the pulse, which is unaffected by the plasma, is at 43 GeV. The core of the pulse, which has lost energy driving the plasma wake, is dispersed partly out of the field of view of the camera. Particles in the back of the bunch, which have reached energies up to 85 GeV, are visible to the right. The pulse envelope exits the plasma with an energy-dependent betatron phase advance, which is consistent with the observed scalloping of the dispersed beam. **b**, Projection of the image in **a**, shown in blue. The simulated energy spectrum is shown in red. The differences between the measured and the simulated spectrum near 42 GeV are due to an initial correlated energy spread of 1.5 GeV not included in the simulations. The horizontal error bar is due to the uncertainty in estimating the deflection angle and the spot size of the beam.

plane 1 (not shown) was 5–7 GeV, which is inconsistent with this explanation. The second possible reason is that the electron hosing instability is so severe that the beam breaks up¹⁶. In the data shown in Fig. 2 there are negligible transverse deflections of the various longitudinal slices of the beam, indicating an absence of the hosing instability. The third possibility is head erosion: the front of the beam expands, because it is not subjected to the focusing force of the ion column. This expansion decreases the beam density, which moves the ionization front backward in the beam frame. Eventually the beam electric field drops below the threshold for plasma formation, terminating the acceleration process before the energy of the drive beam is depleted (see Supplementary Movie 1).

We used simulations to explain the maximum electron energy observed in the experiment. Figure 2b shows a comparison of the measured energy spectrum with one derived from simulations. The electron current distribution is extracted from the energy spectrum of the beam measured upstream of the plasma by comparing it to a phase space simulation using the code LiTrack¹⁷. The wakefield from this current distribution and the propagation of the pulse through the plasma are modelled using the three-dimensional, parallel particle-in-cell (3D-PIC) code QuickPIC¹⁸. QuickPIC includes the effects of field ionization and electron energy loss due to radiation¹⁹ from oscillations in the ion column.

Figure 3a and b shows the simulation output at two different positions in the plasma. At a distance of 12.3 cm, the wake produced by the motion of the plasma electrons resembles that produced in a preformed plasma, because the ionization occurs near the very head of the beam. The expelled plasma electrons return to the beam axis at nearly the same z location. This gives rise to an extremely large spike in the accelerating field. After 81.9 cm one can see the effect of beam head erosion in that the ionization front now occurs further back along the pulse. Even though the wake is formed further back, the peak accelerating field occurs at approximately the same position along the pulse. The transverse size of the pulse ahead of the ionization front is so large that the local beam density has dropped below the useful range in the colour table. However, the modified ionization front causes some blurring of the position at which the returning plasma electrons arrive on the axis, an effect known as phase mixing. This not only reduces the peak accelerating field but also leads to some defocusing of the high-energy beam electrons in this region (see Supplementary Discussion and Supplementary Figs 1–4).

The simulated energy distribution at this point was binned equivalently to the experimental data, as shown in Fig. 2b. The quantitative agreement between the two spectra is good. In the simulation spectrum of Fig. 2b, electrons are accelerated to a maximum energy of 95 GeV. In the experiment, the maximum detectable energy is determined by the spot size at the detection plane, and the highest detected energy is 85 GeV. For the present case, this corresponds to a detection threshold of 3×10^6 electrons per GeV. The mean electron energy of the highest energy bin containing 3×10^6 electrons per GeV in the simulation is shown as a function of position along the plasma in Fig. 3c. Also shown are maximum energies measured in the experiment at 85 and 113 cm for similar electron current profiles. The energy in the simulation increases approximately linearly with propagation distance up to a value of 80 GeV at about 70 cm and then saturates at 85 GeV at 85 cm owing to the phase-mixing effect, which leads to gradual defocusing of the highest energy electrons as mentioned above. As the beam propagates beyond 85 cm, the highest-energy electrons continue to be defocused to such an extent that at 104 cm a significant number of the high-energy electrons are lost to the simulation walls, causing the maximum observed electron energy to drop to 60 GeV. In the experiment, electrons defocused at such angles would not be detectable in the electron spectrometer. It should be noted that no significant wakefield is left beyond 104 cm, because the electron beam core containing the bulk of the particles is completely eroded away.

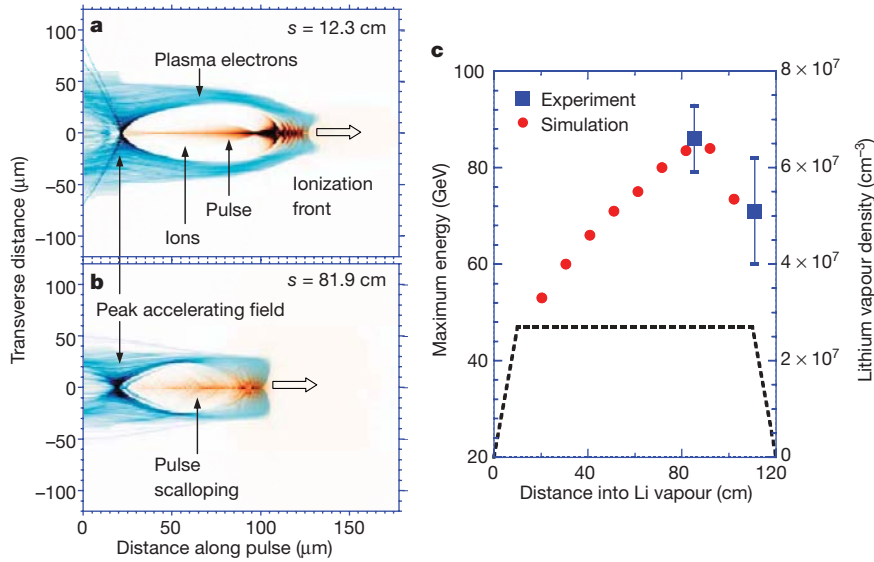


Figure 3 | Simulation of the experiment using the code QuickPIC. The density of the electron pulse (brown) and the plasma electrons (blue) at the distance the beam pulse has propagated $s = 12.3$ cm (a) and 81.9 cm (b) into the plasma on a plane ($y = 0$) through the centre of the simulation box. The pulse travels from left to right. The scalloping features seen at the front of the pulses in a and b are the result of an increasing focusing force as the plasma electrons are still being blown out by the beam electrons. The back of the pulse, entirely within the uniform ion column, is nearly uniformly focused in a. However, the scalloping of the back of the pulse in b—which now has a

The simulations have reproduced the energy spectrum seen in the experiment for an 85-cm-long plasma and elucidated the underlying physical mechanism, head erosion, which leads to the observed saturation of the maximum energy. This effect can be avoided by the use of a lower-emittance beam such that its diffraction length is longer than the plasma length. In that case, the maximum energy gain would be determined by the energy of the drive beam.

Thus, we have produced an accelerating field of 52 GV m^{-1} in a plasma wakefield accelerator and sustained it for 85 cm. The result is in excellent agreement with 3D-PIC simulations. By producing the energy gain of the 3-km-long SLAC accelerator in less than a metre, albeit for a relatively small number of electrons, we have taken an important step towards demonstrating the viability of plasma accelerators for high-energy physics.

METHODS

Electron pulses. A 6-mm-long electron pulse from the SLAC damping ring undergoes three stages of longitudinal compression. In each of these stages, a time-dependent energy is added to the pulse, which is followed by magnetic transport elements that compress the pulse. As a result, the originally 6-mm-long pulses are compressed by a factor of 500 to a minimum length of $12 \mu\text{m}$ (ref. 20). Such a large compression is sensitive to the phases and amplitudes of the klystrons powering the accelerating sections of the linear accelerator, leading to some pulse-to-pulse variation in the bunch length.

The beam has geometric transverse emittances of $\varepsilon_x = 9.5 \times 10^{-10} \text{ m}$ and $\varepsilon_y = 1.2 \times 10^{-10} \text{ m}$. It is focused with a quadrupole doublet to a spot with $10 \mu\text{m}$ radius at the entrance of the plasma. With this beam energy, bunch length and spot size, the corresponding power density is $3 \times 10^{20} \text{ W cm}^{-2}$.

Plasma generation. A column of lithium vapour with a density of $2.7 \times 10^{17} \text{ cm}^{-3}$ is produced in a heat-pipe oven²¹. The lithium vapour is confined by a helium buffer gas, which is in turn separated from the beam-line vacuum by a $50\text{-}\mu\text{m}$ -thick beryllium window upstream and by a $75\text{-}\mu\text{m}$ -thick beryllium window downstream. Lithium was chosen because of the low ionization potential of its first electron (5.4 eV) and the relatively high potential for its two subsequent electrons (76 and 122 eV). In the present experiments the transverse electric field of the ultrashort electron pulses is large enough to field-ionize the first lithium electron over a timescale shorter than the bunch duration. The ADK theory for field ionization²² indicates that full ionization occurs in the volume surrounding the pulse in which the electric field exceeds $\sim 6 \text{ GV m}^{-1}$.

wide range of energies—is due to the energy-dependent focusing through the ion column. Similar features are identifiable in the experimental data of Fig. 2a. c, The maximum observed energy in the experiment (blue squares) for two different plasma lengths is compared to the energy of the particle bin containing 3×10^6 electrons GeV^{-1} (approximately the experimental detection threshold) in simulations (red dots) as a function of distance in the laboratory frame. Also shown is the lithium density profile used for the simulations (dashed line). Vertical error bars are due to the uncertainty in estimating the deflection angle and the spot size of the beam.

Thus, the full ionization extends over a radius of more than $100 \mu\text{m}$ and ionization begins far earlier than the peak of the bunch current. Because the ionization region extends over a radius larger than the plasma collisionless skin depth (c/ω_p , where $\omega_p = (n_e e^2 / \varepsilon_0 m_e)^{1/2}$ is the plasma angular frequency; e is the charge on the electron, ε_0 is the permittivity of free space and m_e is the mass of the electron), the wake is similar to that in a preformed plasma.

Energy measurement. The energy spectrometer consists of a dipole magnet that disperses the electrons vertically according to their momentum p . The dispersion can be closely approximated by a deflection at the centre of the magnet: $\theta_1 = e[BdL/p]$. Using the measured dispersion, its integrated magnetic flux density $|BdL|$ was calculated to be 1.2 T m . In general, all particles in a pulse leave the plasma from a well-defined spot, but with a non-negligible exit angle θ_0 . To discriminate between a vertical exit angle and the deflection by the magnet, the particle distribution is measured at two planes, 86 cm and 186 cm downstream of the centre of the dipole (Fig. 1).

At each of the two planes, the particle distribution is measured by imaging Cherenkov radiation emitted as the electrons pass through a 15-mm-wide air gap established by two silicon wafers (not shown in Fig. 1), positioned at an angle of 45° to the beam. The second wafer acts as a mirror and deflects the Cherenkov light into a lens that images the origin of the light onto a cooled charge-coupled device camera (CCD). The electrons pass the silicon almost unperturbed.

A system of equations is set up relating the offsets at the two planes to two angles, the exit angle at the plasma θ_0 and the deflection angle in the magnet θ_1 (see Fig. 1). For each feature in the spectrum that can be identified on both screens, for instance scalloping of the beam shown in Fig. 2a, this system of equations has been solved for θ_0 and θ_1 , the latter angle giving the particle energy. The highest-energy feature that can clearly be resolved (see Fig. 2a) is used to determine the energy gain for this event. The uncertainty in the energy measurement is dominated by the uncertainty in the determination of the position of this feature.

The images have been corrected at the level of a few per cent for the non-uniform collection efficiency of the optics. Pixel-to-pixel variations in the CCD offset and a common mode have been subtracted; the signal from X-rays that hit the CCD directly has been eliminated.

Simulations. The simulations were done using the quasi-static, three-dimensional, particle-in-cell code called QuickPIC. The three-dimensional computational grid forms a box xyz ($240 \mu\text{m} \times 240 \mu\text{m} \times 260 \mu\text{m}$) in size whose axial coordinate is z - ct . Therefore, the simulation window moves at the speed of light, which is very close to the beam speed in the z direction. The number of grid points is $256 \times 256 \times 512$, respectively. The beam is initialized so that in vacuum, it would focus 15 cm beyond the start of the lithium vapour with a $10 \mu\text{m}$ root-mean-square spot size. The

longitudinal current profile is extracted from the unique LiTrack simulation that matches the experimentally measured beam spectrum produced by the SLAC accelerator. The resulting current profile approximates a gaussian ($\sigma_z \approx 15 \mu\text{m}$) with a small tail. We use 8.4 million particles for the beam and 2.6×10^5 particles for each 'slice' of lithium. In the quasi-static approximation, as the entire beam moves through a slice of gas, the lithium ionizes, the resulting plasma evolves transversely and, to account for the axial motion, the charge on each particle is suitably changed. The resulting plasma forces are stored for each slice and are then used to advance the momentum and position of each beam electron. The beam electrons are advanced every 1.0 mm, which is 1/26th of a betatron wavelength for 42 GeV electrons in the flat density region. The simulations were done on the Apple X-serve Dawson Cluster at UCLA.

1. Tajima, T. & Dawson, J. M. Laser electron accelerator. *Phys. Rev. Lett.* **43**, 267–270 (1979).
2. Chen, P. *et al.* Acceleration of electrons by the interaction of a bunched electron beam with a plasma. *Phys. Rev. Lett.* **54**, 693–696 (1985).
3. Joshi, C. *et al.* Ultrahigh gradient particle acceleration by intense laser-driven plasma density waves. *Nature* **311**, 525–529 (1984).
4. Modena, A. *et al.* Electron acceleration from the breaking of relativistic plasma waves. *Nature* **377**, 606–608 (1995).
5. Gordon, D. *et al.* Observation of electron energies beyond the linear dephasing limit from a laser-excited relativistic plasma wave. *Phys. Rev. Lett.* **80**, 2133–2136 (1998).
6. Umstadter, D. *et al.* Nonlinear optics in relativistic plasmas and laser wake field acceleration of electrons. *Science* **273**, 472–475 (1996).
7. Mangles, S. P. D. *et al.* Monoenergetic beams of relativistic electrons from intense laser–plasma interactions. *Nature* **431**, 535–538 (2004).
8. Geddes, C. G. R. *et al.* High-quality electron beams from a laser wakefield accelerator using plasma-channel guiding. *Nature* **431**, 538–541 (2004).
9. Faure, J. *et al.* A laser–plasma accelerator producing monoenergetic electron beams. *Nature* **431**, 541–544 (2004).
10. Barov, N. *et al.* Propagation of short electron pulses in a plasma channel. *Phys. Rev. Lett.* **80**, 81–84 (1998).
11. Hogan, M. J. *et al.* Multi-GeV energy gain in a plasma-wakefield accelerator. *Phys. Rev. Lett.* **95**, 054802 (2005).
12. Katsouleas, T. Physical mechanisms in the plasma wake-field accelerator. *Phys. Rev. A* **33**, 2056–2064 (1986).
13. Bruhwiler, D. *et al.* Particle-in-cell simulations of tunneling ionization effects in plasma-based accelerators. *Phys. Plasmas* **10**, 2022–2030 (2003).
14. Rosenzweig, J. B. *et al.* Acceleration and focusing of electrons in two-dimensional nonlinear plasma wake fields. *Phys. Rev. A* **44**, R6189–R6192 (1991).
15. Clayton, C. E. *et al.* Transverse envelope dynamics of a 28.5-GeV electron beam in a long plasma. *Phys. Rev. Lett.* **88**, 154801 (2002).
16. Dodd, E. S. *et al.* Hosing and sloshing of short-pulse GeV-class wakefield drivers. *Phys. Rev. Lett.* **88**, 125001 (2002).
17. Bane, K. L. F. & Emma, P. LiTrack: a fast longitudinal phase space tracking code with graphical user interface. Stanford Linear Accelerator Center Report No. SLAC-PUB-11035 (SLAC, Menlo Park, California, 2005).
18. Huang, C. *et al.* QUICKPIC: A highly efficient particle-in-cell code for modeling wakefield acceleration in plasmas. *J. Comput. Phys.* **217**, 658–679 (2006).
19. Johnson, D. K. *et al.* Positron production by X rays emitted by betatron motion in a plasma wiggler. *Phys. Rev. Lett.* **97**, 175003 (2006).
20. Krejcik, P. *et al.* Commissioning of the SPPS linac bunch compressor. *Proceedings of the Particle Accelerator Conference (12–16 May, 2003, Portland, Oregon)* 423–425 (IEEE, Piscataway, New Jersey, 2003).
21. Muggli, P. *et al.* Photo-ionized lithium source for plasma accelerator applications. *IEEE Trans. Plasma Sci.* **27**, 791–799 (1999).
22. Ammosov, M. V. *et al.* Tunnel ionization of complex atoms and of atomic ions in an alternating electromagnetic field. *Sov. Phys. JETP* **64**, 1191–1194 (1986).